RSC Advances

PAPER

View Article Online
View Journal | View Issue

Open Access Article. Published on 25 November 2025. Downloaded on 1/19/2026 4:08:04 AM.
This article is licensed under a Creative Commons Attribution-NonCommercial 3.0 Unported Licence.

Check for updates

Cite this: *RSC Adv.*, 2025, **15**, 46553

Eco-friendly magnetic activated carbon modified with green tea extract for efficient adsorption of thiazine and azo dye contaminants from water

Muhammad Usama,[a] Sawaira Atta,[a] Muhammad Naveed Qasim,[a] Afnan Qabil Alshammari,[b] Abdullah K. Alanazi,[c] Naseem Ahmad Khan,[a] Muhammad Mateen *[d] and Muhammad Nadeem Akhtar *[a]

Received 20th August 2025
Accepted 16th November 2025

DOI: 10.1039/d5ra06187c

rsc.li/rsc-advances

This study describes the development of maghemite supported activated carbon (MAC) loaded with green tea extract (GTE), as a high-performance adsorbent for the effective extraction of both thiazine dye (methylene blue, MB) and an azo dye (methyl orange, MO) from water. The composite MAC–GTE was prepared through a straightforward wet-chemical method and demonstrated outstanding dye uptake of 491.47 mg g^{-1} for MB at pH 9 and 337.89 mg g^{-1} for MO at pH 3.0, with removal efficiency of 98.29% and 90.10%, respectively. Adsorption data showed stronger agreement with the Freundlich isotherm and pseudo-second-order kinetics, indicating multilayer chemisorption. The composite showed strong magnetic response enabling easy magnetic separation and successful recycling. The synergistic combination of maghemite and green tea extract polyphenols enhanced the surface reactivity and accessibility of active sites, suggesting that MAC–GTE may be a promising, and sustainable material for dyes removal applications.

1. Introduction

Human survival depends on water, vital for many different spheres of life. Drinking water is necessary for human consumption, hydration and digestion, hygiene, sanitation, and medical uses.[1] Dyes, heavy metals, drugs, and organic compounds may cause water pollution. Before being disposed of these highly toxic, non-biodegradable, and carcinogenic contaminants must be eliminated from wastewater.[2] Dyes are more common and have adverse effects not only for humans but also for aquatic life. Several methods, such as physical, chemical, and biological methods have been explored in the literature to remove wastewater pollutants.[3,4] Apart from the textile industry, other industries, including food additives, mining, batteries, paper, plastics, paints, electroplating, agricultural and medical sectors, can also release dyes into the water system.[5] In trace amounts, these can impair the functioning of the brain, blood, liver, kidneys, and metabolic human systems. They can be removed from wastewater using solvent extraction, electrodialysis, ion exchange, chemical precipitation, ultrafiltration, coagulation, flocculation, and adsorption.[6,7] Dyes in water can harm the environment and human health and can affect the human body by causing cancer, allergies, and organ damage.[8] To remove the organic dyes from the aqueous system, adsorption is one of the most useful techniques in which the dye molecules are attracted to the adsorbent surface through van der Waals forces, and hydrogen bonding.[9] Moreover, its molecules penetrate the adsorbent pores and bind to its surface, and the adsorbent's high surface area and porosity enhance the dye's adsorption. Chemical reactions may also form a strong bond between the dyes and adsorbents.[10] Methylene blue (MB) is a synthetic dye with a deep blue color, and its structure is well known for allowing accurate adsorption modeling.[11] Besides that, MB is also used for various textile, paper, and biological staining purposes, and could be suitable for adsorption onto negatively charged surfaces. Furthermore, it is also widely used as a model pollutant in adsorption research studies due to its well-defined structure and properties.[12] Methyl orange (MO) is a synthetic azo dye with a bright orange color and is used as a coloring substance in the textile, paper, and leather industries. MO is a weak acid that, depending on pH, can exist in several ionic forms, and MO removal from wastewater is essential since it is poisonous and carcinogenic.[13] Activated carbon is one of the most widely used systems for various industries due to its high adsorption capacity and versatility. Usually, MB shows more accessible results than MO in adsorption studies using activated carbon because MB is

[a]Division of Inorganic Chemistry, Institute of Chemistry, The Islamia University of Bahawalpur, Bahawalpur 63100, Pakistan. E-mail: nadeemchem@yahoo.com; m.nadeemakhtar@iub.edu.pk

[b]Department of Chemistry, College of Science, Jouf University, P. O. Box 2014, Sakaka, Saudi Arabia

[c]Department of Chemistry, College of Science, Taif University, Saudi Arabia

[d]Chongqing Key Laboratory of Catalysis and New Environmental Materials, College of Environment and Resources, Chongqing Technology and Business University, Chongqing 400067, China. E-mail: mateenchem@hotmail.com

© 2025 The Author(s). Published by the Royal Society of Chemistry

Open Access Article. Published on 25 November 2025. Downloaded on 1/19/2026 4:08:04 AM.
This article is licensed under a Creative Commons Attribution-NonCommercial 3.0 Unported Licence.

a cationic dye while MO is an anionic dye. MB and MO molecules diffuse onto the surface of the activated carbon, and dye molecules are trapped and held on the surface. Furthermore, the high degree of selectivity of activated carbon makes it a very efficient way of targeting particular chemicals or groups of contaminants in contaminated water.[14]

Activated carbon is a very efficient adsorbent material due to its high surface area, porous nature, chemical stability, and affinity towards molecules, making it a widely used material in adsorption processes.[15] The adsorbents used largely affect the selectivity of the adsorption process and the adsorption capacity. Poor selective sorption and low adsorption capacities are the factors that have limited the applications of typical adsorbents like activated carbon.[16] Activated carbon undergoes adsorption of toxic pollutants, exhibits a high affinity towards attracting molecules, and is put into various applications like water treatment, air purification, medical treatment, and various industrial applications.[17] Economic viability in producing the material of activated carbon from waste biomass enhances its appeal for use in the treatment of wastewater. Abundant availability of wastes improves the financial feasibility and sustainability of the method.[18]

Various plant extracts like neem, aloe vera, and moringa have also been explored for the green synthesis of magnetic activated carbon, thanks to their natural reducing and stabilizing constituents.[19–21] However, these extracts usually contain low concentrations of reactive polyphenols with limited stability during the synthesis process. On the other hand, green tea extract is very rich in catechin-type polyphenols such as EGCG, EC, ECG, and EGC, which promote particle dispersion, introduce oxygenated functional groups, and enhance adsorption efficiency.[22] Hence, green tea extract was chosen in this study as a practical and very efficient bio-reducing and surface-functionalizing agent for the production of magnetic activated carbon.

Accordingly, in the view of the facts mentioned above, we have prepared tea extract-derived magnetic activated carbon (MAC–GTE) composite material by wet-chemical and post ultrasonication approaches. Besides introducing oxygen-rich functional groups, improving nanoparticle dispersion, and facilitating synergistic interactions, the addition of green tea extract during Fe_2O_3/activated carbon composite synthesis provides a green and sustainable route and improves the adsorption performance of the composite. The overall adsorption efficiency of the composite is improved due to the polyphenolic compounds, mainly catechins such as epigallocatechin gallate (EGCG), epicatechin (EC), epicatechin gallate (ECG), and epigallocatechin (EGC) present in green tea, which contribute toward increased surface reactivity and binding affinity toward target pollutants. GTE plays multiple roles and enhanced the pollutant adsorption features of the MAC. Extensive dye adsorption capabilities of MAC–GTE composite against MB and MO dyes were investigated. Further, we also presented an in-depth study on the various factors affecting adsorption and a detailed kinetic investigation.

Although many adsorbents have been explored for dyes removal, there is still a gap in developing efficient, economically viable, and green materials. Most of the existing adsorbents developed so far possess some drawbacks, such as low adsorption capacity, poor kinetics, and difficulty in regeneration. Additionally, modifying activated carbon with environment-friendly materials, such as green tea extract, to enhance dye removal efficiency, particularly thiazine and azo dyes, has rarely been explored. The present study closes the gaps by presenting a new method of activated carbon modification using green tea extract. These green modifications will not only enhance the adsorption capacity of dyes contaminants but also introduce magnetic properties into the material for its easy recovery, proposing various environmental and economic advantages.

2. Experimental work

2.1 Material and method

Iron nitrate nonahydrate $Fe(NO_3)_3(H_2O)_9$ and sodium hydroxide (NaOH 99%) were sourced from Merck, Germany. Methyl blue (99%), methylene orange (90%), green tea extracts, and activated carbon were purchased from Sigma-Aldrich. The reagents of all of these compounds were utilized without subsequent purification.

2.2 Synthesis of Fe_2O_3–AC

Activated carbon (5 g) was added to 100 mL of DI-H_2O and was sonicated for about 1 hour. The 0.1 M $Fe(NO_3)_3(H_2O)_9$ (100 mL) was introduced in the above solution. The combination underwent stirring for an hour at a temperature of about 70–80 °C. Under vital agitation at 80 °C, the stirred NaOH (0.2 M) solution was gradually introduced into the solution above, one drop at a time, until the pH attained 10–11. The expulsion was further stirred at 80 °C for 1 hour and kept at room temperature for 24 hours. The iron oxide/activated carbon, also mentioned as magnetically active carbon (MAC), was separated using a magnet and rinsed with DI-H_2O and ethanol until its pH reached neutral. Subsequently, the material was desiccated in an oven at 80 °C for 12 hours. MAC sample was crushed in a mortar and pestle after dehydrating and finally stored.

2.3 Synthesis of MAC–GTE composite

The composite (MAC–GTE) was synthesized by simple wet-chemical followed by ultra-sonication approach. Fig. 1 shows the schematic illustration of the synthesis of MAC–GTE composite material.

The MAC–GTE composite was synthesized through a simple wet-chemical process followed by ultrasonication. Green tea extract (GTE) was first prepared by sonicating 2.00 g of dried green tea leaves in 50 mL of distilled water at 50 °C for 30 min. The mixture was filtered to obtain a clear extract, which was stored at low temperature until further use.

For composite formation, the maghemite-activated carbon (MAC) precursor dispersion (50 mL) was mixed gradually with 50 mL of the ethanolic green tea extract under continuous stirring. The pH of the mixture was then adjusted to 11 by the dropwise addition of 0.2 M NaOH solution, and stirring was

 © 2025 The Author(s). Published by the Royal Society of Chemistry

Open Access Article. Published on 25 November 2025. Downloaded on 1/19/2026 4:08:04 AM.
This article is licensed under a Creative Commons Attribution-NonCommercial 3.0 Unported Licence.

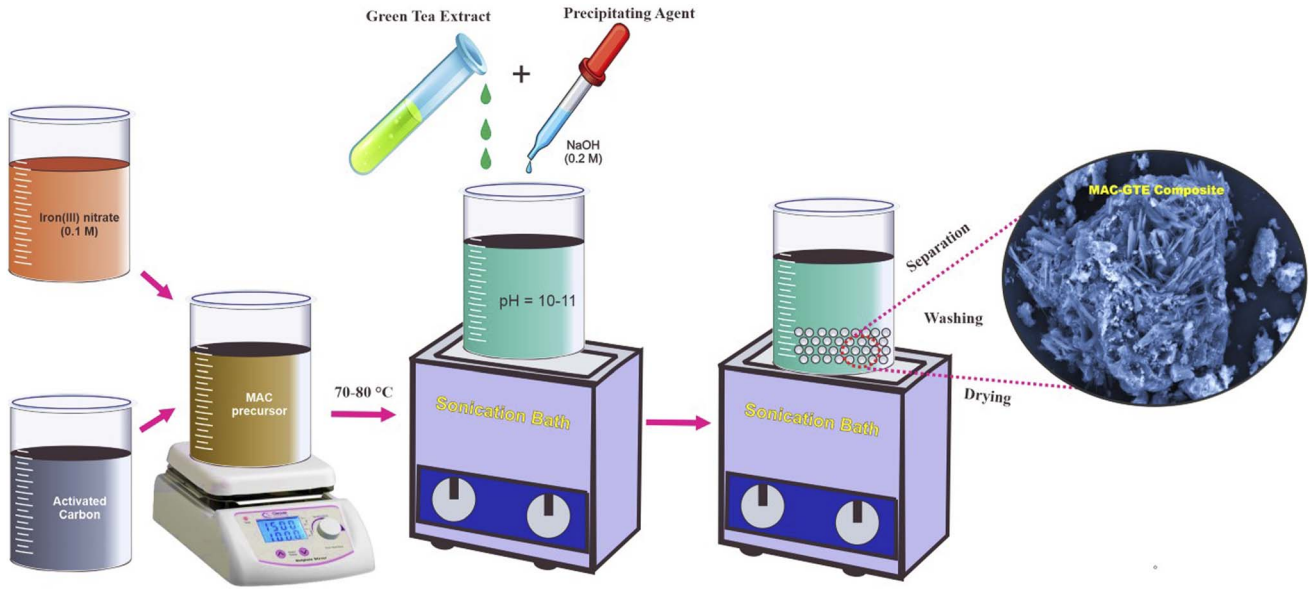

Fig. 1 Synthesis scheme of magnetic activated carbon-green tea extract (MAC–GTE).

continued for 1 h to ensure complete interaction between the components. The resulting MAC–GTE composite was separated magnetically, washed repeatedly with deionized water and ethanol until neutral pH, and finally dried at 40 °C to preserve the heat-sensitive polyphenols that provide active adsorption sites. In contrast, the pristine MAC was dried at 80 °C, as its inorganic-carbon framework is thermally stable and unaffected at this temperature.

For clarity, the quantitative ratios of the materials used are summarized as follows: 5.00 g of activated carbon was used per synthesis with 100 mL of 0.10 M $Fe(NO_3)_3$ solution (0.0100 mol Fe), corresponding to a theoretical Fe_2O_3 yield of 0.798 g (≈16 wt% relative to AC). The green tea extract prepared from 2.00 g of dry leaves yielded approximately 0.40 g of soluble extractives (~20% extraction yield), resulting in an estimated GTE : AC mass ratio of 0.40 : 5.00 (≈8 wt%).

2.4 Characterization of as-synthesized materials

The prepared material was characterized by a UV-visible spectrophotometer (Cecil Aquarius 7400 UV visible spectrophotometer), FT-IR (TENSOR 27 model 2010 of Bruker), PXRD (Bruker D8), SEM (ProX G6 Desktop) and TGA (STA 449 F1 Jupiter).

2.5 Adsorptive batch experiment

Batch adsorption experiments were conducted to evaluate the adsorption physiognomies of MAC–GTE. A 20 ppm dye solution was prepared to assess the effect of pH on the removal efficiency through pH analysis, with the highest efficiency recorded at pH 9. Following this analysis, a contact time experiment was carried out at pH 9, measuring removal efficiency after 20 minutes. However, the composite demonstrated peak efficiency after 140 minutes. Subsequently, experiments were conducted with varying initial dye concentrations of 20, 30, and 40 ppm. Additionally, removal efficiency was assessed at different temperatures (25 °C, 35 °C, 45 °C). The composite exhibited an adsorption capacity of 491.47 mg g^{-1} for MB at 20 ppm, surpassing the 337.89 mg g^{-1} capacity for MO at the same concentration, with removal efficiencies of 98.29% and 90.10%, respectively. A UV-visible spectrophotometer was utilized to determine the concentrations of MB and MO at their respective lambda max values of 664 nm and 462 nm. Beer–Lambert law was utilized for the determination (extinction coefficient) through the findings of a UV-visible spectrophotometer. Eqn (1) and (2) were leveraged to ascertain the composite capacity for adsorption and removal efficiency of MB and MO, respectively.[23,24]

$$\text{Adsorption capacity} = \frac{(C_o - C_e)V}{m} \tag{1}$$

$$\text{Removal efficiency} = \frac{(C_o - C_e)}{C_o} \times 100 \tag{2}$$

where C_o and C_e are initial and equilibrium concentrations (mg L^{-1}) of MB and MO, sequentially, while V is the volume of a solution (L) and m is the amount of adsorbent (mg). Various kinetic models, such as pseudo-1st-order (PFO), pseudo-2nd-order (PSO), and liquid film diffusion (LFD), were implemented to understand the adsorption mechanism. Eqn (4)–(6) represent these models correspondingly.[25]

$$K_1 = \frac{\ln q_e - \ln(q_e - q_t)}{t} \tag{3}$$

$$K_2 = \frac{q_t}{t}\left(\frac{1}{q_e^2} + \frac{t}{q_e}\right) \tag{4}$$

$$K_F = \frac{A - \ln\left(1 - \frac{t}{q_e}\right)}{t} \tag{5}$$

Open Access Article. Published on 25 November 2025. Downloaded on 1/19/2026 4:08:04 AM.
This article is licensed under a Creative Commons Attribution-NonCommercial 3.0 Unported Licence.

K_1, K_F, and K_2 are the PSO, liquid-film diffusion model adsorption rate constant (h^{-1}), and the PSO adsorption rate constant (g mg^{-1} h^{-1}), respectively. Meanwhile, q_e and q_t represent the capacity for adsorption at equilibrium and at time t, respectively. In addition to this, to study the adsorption layer mechanism, several adsorption isotherm models were examined, including the Langmuir model, the Freundlich model, and the Temkin model. Eqn (6)–(8) explain three different isothermal models.[26,27]

$$\frac{C_e}{q_e} = \frac{C_e}{q_{max}} + \frac{1}{q_{max}K_L} \tag{6}$$

$$\ln q_e = \frac{1}{n} \ln C_e + \ln K_F \tag{7}$$

$$q_e = K_T \ln C_e + K_T \ln f \tag{8}$$

Here, K_L, K_F, and K_T are the adsorption constants for Langmuir (L mg^{-1}), Freundlich adsorption constant, and Temkin binding constant (L mg^{-1}), correspondingly.

3. Results and discussion

3.1 Structure analysis

X-ray diffraction (XRD) techniques have been exploited to examine the structural attributes of the AC, MAC, and MAC–GTE materials (Fig. 2a). The XRD pattern of AC consists of two broad humps, indexed as the (002) and (100) Miller planes.[28] The broad and less intense nature of the peaks may be attributed to the small graphitic domains and the lack of long-range ordered structure, respectively.[29,30] In addition to the broad bump characteristic of activated carbon, the XRD pattern of the MAC sample displays six distinct diffraction peaks that are in a perfect agreement with the standard JCPDS card #39-1346, which serves as confirmation of the maghemite phase's cubic crystal structure (γ-Fe_2O_3).[31] The face-centered cubic (FCC) structure of the maghemite phase is further validated by the fact that all of the Miller indices (h, k, l) are either all even or all odd.

In the XRD pattern of the MAC–GTE composite, a broad hump observed between 15° and 28° can be attributed to the coexistence of amorphous activated carbon and organic functionalities (hydroxyl, carbonyl, carboxyl, π–π interactions, *etc.*) imparted by the green tea extract (GTE).[32,33] The attenuation of the maghemite diffraction peaks in the MAC–GTE pattern is due to the amorphous GTE-derived organic layer, which forms an approximately 8 wt% surface coating on the activated carbon (see quantitative ratios in Section 2.3). The Fe_2O_3 loading corresponds to roughly 16 wt% relative to the activated carbon, consistent with the theoretical stoichiometry.

The incorporation of GTE does not alter the core crystalline structure of maghemite but partially masks its diffraction signals because the surface is covered by organic moieties. Moreover, the bioactive polyphenolic compounds in GTE interact with the maghemite surface during synthesis, acting as natural capping and stabilizing agents that restrict crystal growth.[34] As a result, the diffraction peaks become slightly broader, indicating a reduction in crystallite size. Using Scherrer's equation,[35] the crystallite size (D) decreased from 12.39 nm (MAC) to 11.08 nm (MAC–GTE), confirming the influence of GTE on crystal nucleation and growth.

$$D = \frac{K\lambda}{\beta \cos \theta} \tag{9}$$

The X-ray density values (MAC = 2.84 g cm^{-3}; MAC–GTE = 2.52 g cm^{-3}) and corresponding crystallite sizes were used to estimate the specific surface area (SSA) according to the method of Rashid *et al.* and others.[36,37]

$$\mathrm{SSA} = \frac{6000}{\rho_{\text{X-ray}} \times D} \tag{10}$$

The calculated SSA increased from 170 m^2 g^{-1} (MAC) to 214 m^2 g^{-1} (MAC–GTE) after surface functionalization,

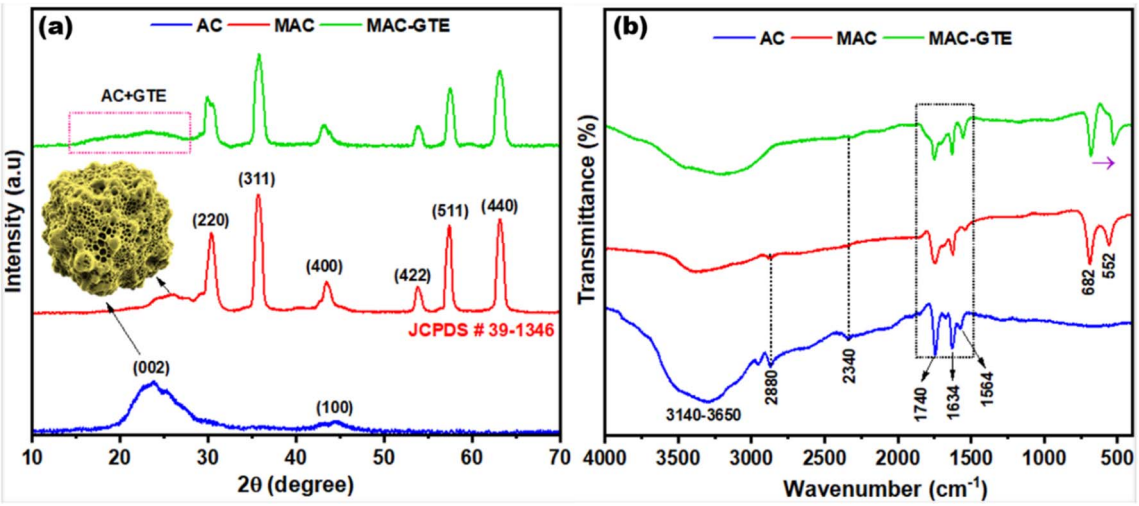

Fig. 2 (a) XRD and (b) FTIR of AC, MAC, and MAC–GTE samples.

 © 2025 The Author(s). Published by the Royal Society of Chemistry

Open Access Article. Published on 25 November 2025. Downloaded on 1/19/2026 4:08:04 AM.
This article is licensed under a Creative Commons Attribution-NonCommercial 3.0 Unported Licence.

demonstrating that GTE incorporation enhanced the accessible active sites. This improved surface area and the synergistic hybrid structure make the MAC–GTE composite a promising adsorbent for the efficient removal of aqueous pollutants.[38]

In order to identify the functional groups and lattice vibrations present in the prepared samples, FTIR was performed within the 4000–400 cm^{-1} range. This spectral window is particularly well-suited for the detection of the organic signatures from green tea extract (GTE), the characteristic Fe–O lattice vibrations in maghemite, and the stretching and bending modes of surface functionalities in activated carbon. The spectrum of AC shows O–H stretching (3140–3650 cm^{-1}) and bending (1634 cm^{-1}) vibrations, both of which can arise from surface hydroxyl groups, adsorbed water molecules, and hydroxyl functionalities associated activated matter.[39] The spectrum also shows a weakened band at approximately 2880 cm^{-1}, corresponding to aliphatic C–H stretching vibrations from residual hydrocarbon moieties, and a distinct peak at around 2340 cm^{-1}, attributed to the asymmetric stretching of CO_2 molecules adsorbed from the atmosphere.[40,41] More importantly, in spectrum, a medium-intensity band at 1564 cm^{-1} corresponds to aromatic C=C stretching, while a more intense band at 1740 cm^{-1} is assigned to C=O stretching from carbonyl or carboxylic groups introduced during activation;[42,43] the higher intensity of the C=O band is due to its polar nature and the stronger variation in dipole moment compared to C=C. These structural features reflect the existence of aromatic domains, oxygen-containing functional groups, and atmospheric adsorbent in the AC.

The MAC sample's spectrum, apart from the containing characteristic bands of AC, also two distinct bands; a strong one at 630 cm^{-1} (Fe–O stretching at tetrahedral sites) and a weaker one at 580 cm^{-1} (Fe–O stretching at octahedral sites).[44] The diminished intensities of the AC bands may ascribe to the partial surface coverage of carbonaceous matrix with maghemite particles. The presence of these Fe–O bands in conjunction with the diminished AC peaks offers compelling spectroscopic evidence for the effective incorporation of maghemite onto the activated carbon surface.

The MAC–GTE spectra display a reduction in wavenumbers for both Fe–O bands, which suggests a decrease in the strength of the Fe–O bond, and this in turn may be a result of the presence of phenolic groups from GTE that have coordinated with the Fe^{3+} ions on the surface.[45] It is very likely that such bonding will make the Fe–O bond less strong by changing the electron density around it. The connectivity of the polyphenolic hydroxyl groups in GTE through hydrogen bonds is signaled by the broad O–H stretching band's extension towards lower wavenumbers.[46] The GTE presence has a major impact on the absorption bands in the range of 1800–1500 cm^{-1}. The reason behind this is the combined contributions from the various aromatic rings, hydroxyls, and carbonyls of catechins as well as other flavonoids, which are the sources of AC signals. The more powerful O–H bending indicates the presence of more hydrogen-bonded hydroxyls, whereas the stronger C=O peak is due to the presence of ester and oxidized phenolic groups. The larger C=C band is a representation of the GTE aromatic structures. The spectral changes mentioned above point to the presence of efficient organic–inorganic interaction and surface functionalization in the MAC–GTE composite.

The disappearance of the 2880 cm^{-1} C–H stretching band in the MAC–GTE composite indicates that aliphatic groups were masked or altered through interactions with GTE's polyphenols.

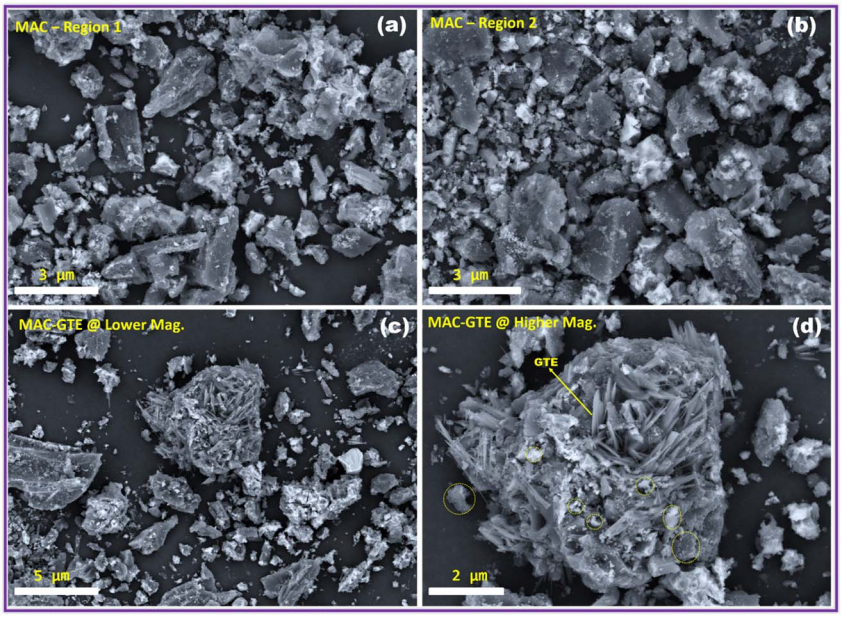

Fig. 3 SEM images of (a and b) MAC (two regions at comparable magnification) and (c and d) MAC–GTE at lower and higher magnification, respectively.

Open Access Article. Published on 25 November 2025. Downloaded on 1/19/2026 4:08:04 AM.
This article is licensed under a Creative Commons Attribution-NonCommercial 3.0 Unported Licence.

This confirms successful surface modification and formation of new oxygen-containing functional groups.

3.2 Morphological analysis

Fig. 3a and b illustrates SEM images of the magnetically activated carbon (MAC) particles at comparable magnification, thereby verifying that the activated carbon matrix material is primarily composed of predominantly microparticles with an irregular shape and non-uniform dispersion pattern.

The irregular surface texture of the AC is also decorated with magnetite particles. The magnetite particles are smaller and are prone to being distributed among the larger AC particles or randomly distributed over their surface. In order to emphasize the efficient deposition of magnetite onto AC, this configuration was implemented, thereby improving the surface character and the presence of active sites for subsequent contacts. In comparison, the SEM images of a MAC–GTE (Fig. 3c and d) at lower (lower left) and higher magnifications (lower right). The MAC sample's heterostructure and hetero-sized patches interwoven with almost-linear and flake-like structures (GTE) to form a nest like structure, as evident in Fig. 3d. The SEM analysis propose that the composite material, which is the combination of magnetite, activated carbon, and GTE, have been successfully prepared. The adsorption efficacy and functionality of the material are enhanced due to the appeared coated surface with GTE-derived organic flakes, which results in increasing roughness and available binding sites.

3.3 UV-visible spectroscopy

The optical properties of MAC and MAC–GTE composites were examined *via* their UV-vis absorption spectra recorded in the wavelength window from 300–900 nm, as given in Fig. 4a and b, respectively.

The addition of green tea extract (GTE) to the MAC composite results in enhanced absorption within the 300–400 nm range. The flavonoids and catechins constituting GTE are likely responsible for such enhancement in the absorption, as these chemical moieties exhibit strong UV-range π–π transitions. This is most likely due to the presence of phenolic compounds occurring in GTE such as flavonoids and catechins. These compounds demonstrate strong UV-range π–π transitions, which assist in the MAC–GTE composite's increased absorption. The phenolic compounds from GTE likely bound to the surface of the magnetite particles, which is perhaps the reason for increased absorption in that region. In the UV region, optical absorption is more noticeable, and as one moves toward the lower wavelength boundary, it becomes less noticeable. The significant absorption peaks within the near infrared range of 700–900 nm for both MAC and MAC–GTE composites are likely due to the d–d transitions of Fe ions in magnetite which confirms the presence of iron complexes in both samples. The MAC–GTE composite UV-vis absorption profile is more uniform which indicates synergistic interaction between GTE and magnetite and may enhance the effectiveness of the composite for applications in adsorption and catalysis. We agreed that the slight noise in the 800–900 nm region may arise from instrumental limits, while the weak absorption around 850 nm corresponds to Fe^{3+} d–d transitions, indicating interaction with GTE polyphenols. XPS and Raman analyses will be considered in future work for more conclusive evidence.

3.4 Thermogravimetric analysis (TGA)

To determine the thermal stability, the TGA measurements of Fe–AC and MAC–GTE were studied by monitoring the weight change that occurred when the sample was heated in an inert atmosphere. Fig. 5 shows the mass loss curves of MAC and MAC–GTE respectively. In Fig. 5a, MAC shows three-step decomposition, as mass loss curves indicated. The observed maximum weight loss of 4.8% occurred at 350 °C, which is mainly due to the decomposition of the carbonaceous material. The second weight loss is 3.94%, occurred at 657 °C and might be due to the decomposition of organic components in the activated carbon matrix.[47] The third weight loss, which is about 3.24%, occurs at 880 °C and is associated with either the

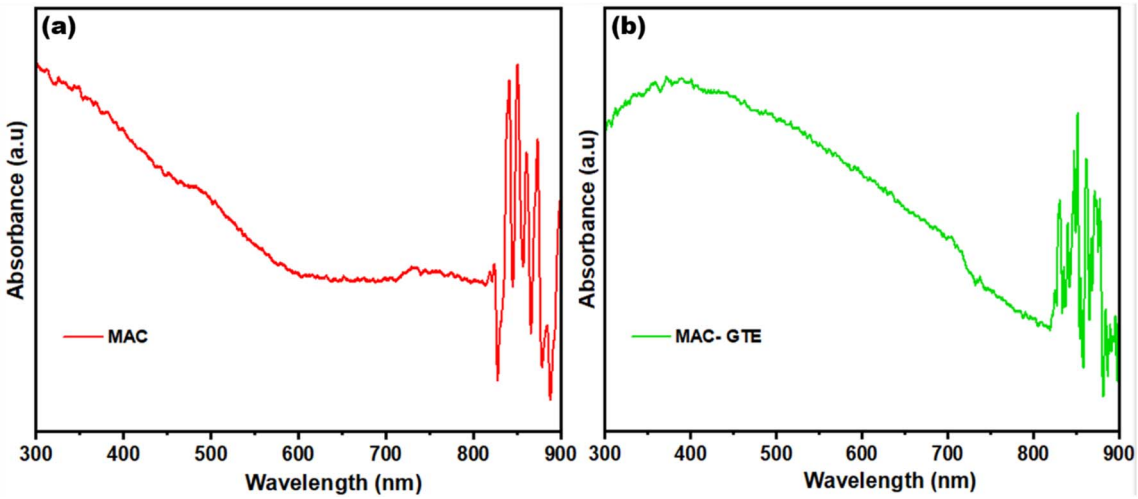

Fig. 4 UV-vis absorption spectra of MAC (a) and MAC–GTE (b) composites.

 © 2025 The Author(s). Published by the Royal Society of Chemistry

Open Access Article. Published on 25 November 2025. Downloaded on 1/19/2026 4:08:04 AM.
This article is licensed under a Creative Commons Attribution-NonCommercial 3.0 Unported Licence.

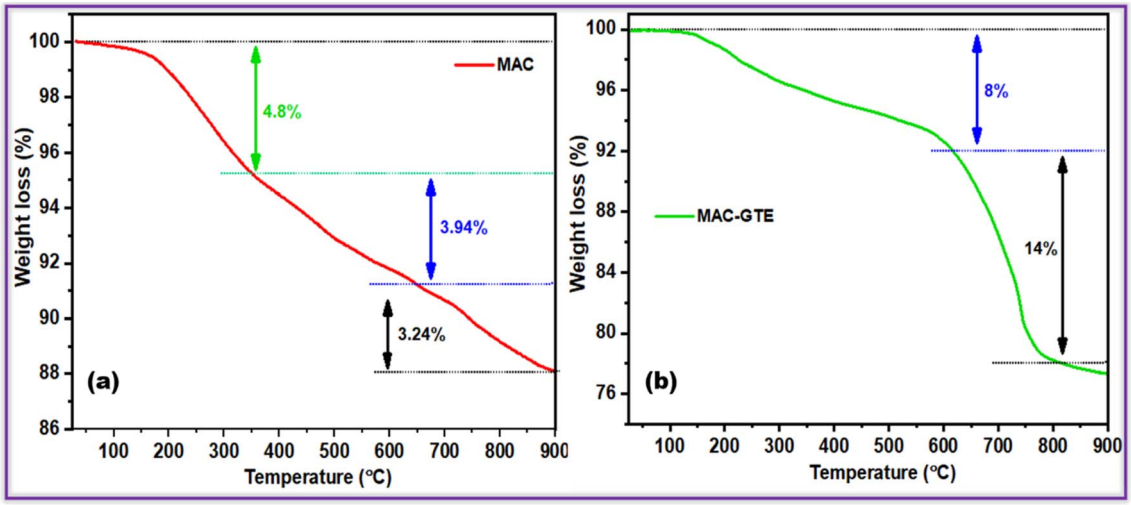

Fig. 5 TGA spectra of MAC (a) and MAC–GTE (b) composites.

breakdown of the carbon structure or the oxidation of residual carbon. The material reaches its final stage of thermal decomposition at 880 °C. On the other hand, the decomposition of MAC–GTE (Fig. 5b) also occurred in two main and distinct stages. The first weight loss is of almost 8% and extended up to 600 °C, representing the physicochemical dehydration and the decomposition of primary carbonaceous structures.[48] The major weight loss of 14% extended up to 800 °C, suggesting the pyrolytic degradation of the carbon matrix and Fe-catalyzed structural decomposition. The material reaches its final thermal breakdown and stabilization at 900 °C.

3.4.1 Interpretation of weight loss. MAC and MAC–GTE thermograms show a three and two steps mass-loss pattern. The desorption of light volatiles and physisorbed water is responsible for the first, low-temperature loss (<∼150–200 °C). The second stage (about 200–500 °C) is associated with the thermal breakdown of labile organic matter and oxygenated surface functionalities (carboxyl, phenolic, and lactone groups); in MAC–GTE, this stage is accelerated by the breakdown of the green-tea polyphenol coating. The more refractory carbon matrix (char) oxidizes or burns, causing the third, high-temperature loss (>∼500 °C). The more noticeable high-temperature mass loss seen for the iron-impregnated and GTE-coated samples can be explained by the fact that iron species can promote carbon oxidation. These TGA findings align with data from SEM-EDS (iron present) and FTIR (surface oxygenated groups).

The interaction between GTE and MAC involves hydrogen bonding, π–π stacking, and Fe–O coordination, where GTE polyphenols bind to MAC's surface groups and Fe^{3+} ions. The chemical interactions that take place give the materials better thermal and chemical stability which in turn allow them to endure a number of adsorptions–desorption cycles. The MAC–GTE composite has a strong and stable organic–inorganic interface that is further evidenced by FTIR technique, which tells the characteristic shifts in the O–H and C=O stretching regions after GTE functionalization. Unlike activated carbon from green tea which loses most of the polyphenolic functionalities during pyrolysis, the MAC–GTE composite keeps those bioactive groups by using a mild surface modification of maghemite-supported activated carbon. This method results in an increased surface reactivity, higher adsorption capacity and magnetic separability of a bio-inspired hybrid material that shows much better dye removal efficiency and recyclability as compared to conventional adsorbents.

3.5 Factors affecting adsorption

3.5.1 Effect of time and pH. The percentage efficiency and effectiveness were observed after 20 minutes intervals using 10 mg of MAC–GTE composite. As time passes, the diffusion rate of dyes onto the surface of the composite material increases, enhancing adsorption effectiveness and efficiency. Many active sites are present in the MAC–GTE composite surface, which attract the MB and MO molecules and increase the adsorption efficiency. The maximum adsorption effectiveness and removal efficiency for MB recorded 491.47 mg g^{-1} and 98.29%, respectively, which is larger than 337.89 mg g^{-1} and 90.10% of MO after 140 min, as shown in Fig. 6a and b.

The pH of the solution is also an important parameter affecting dyes' adsorption because pH controls the adsorbent–adsorbate interactions.[49] Usually, the efficiency of dye adsorption by synthesized adsorbent depends on the solution's pH. At ambient temperature, 20 ppm of methylene blue (adsorbent dosage of 10 mg) and 15 ppm of methyl orange (adsorbent dosage of 10 mg) were used to study the influence of pH of MB and MO on adsorption over the MAC–GTE composite. The pH range between 2 and 12 was examined, as shown in Fig. 6c and d. At low pH (3), the MAC–GTE composite surface has a positive charge due to protonation, while methyl orange has a negative charge (anionic dye), which leads to an efficiency of 90.10%. It is reported at lower pH (under acidic conditions), MO emerges in quinoid form, while at higher pH,

Open Access Article. Published on 25 November 2025. Downloaded on 1/19/2026 4:08:04 AM.
This article is licensed under a Creative Commons Attribution-NonCommercial 3.0 Unported Licence.

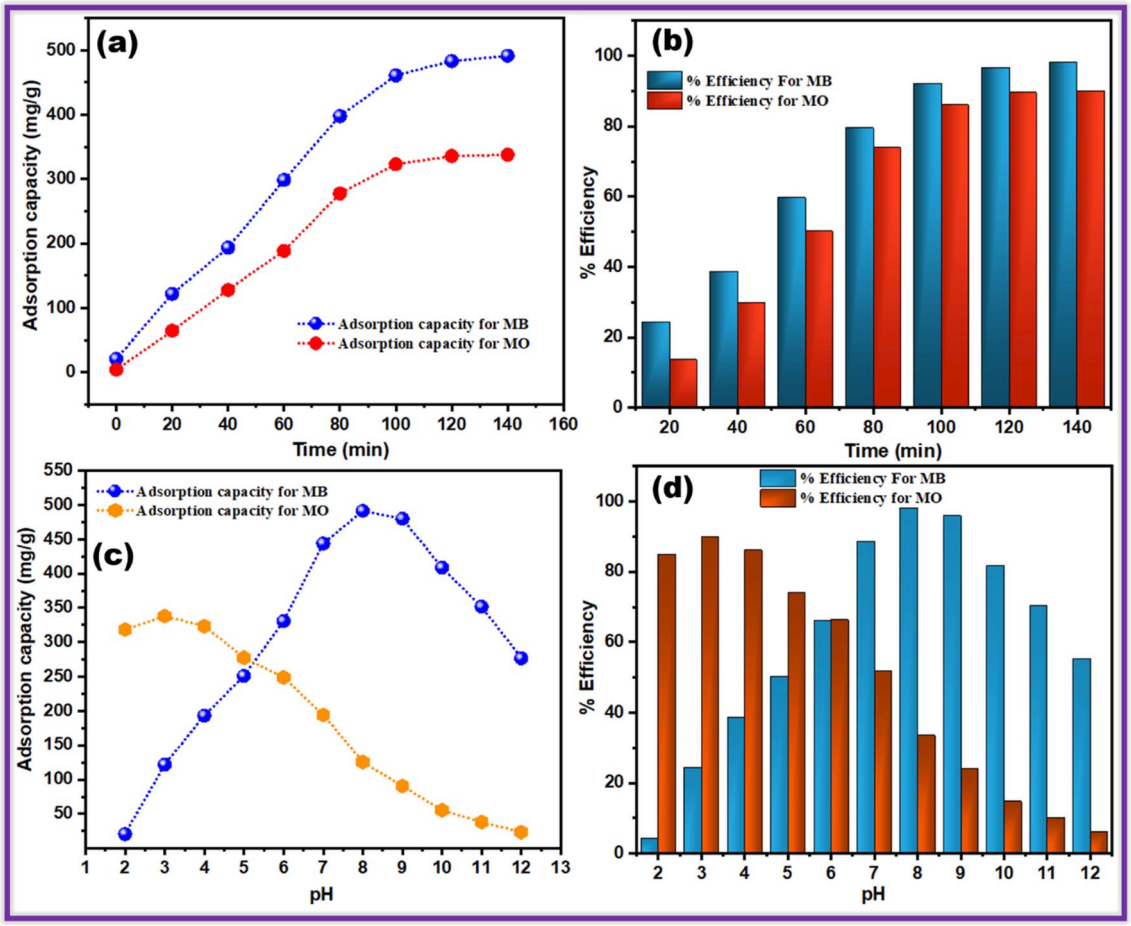

Fig. 6 Adsorption study of methylene blue (MB) and methyl orange (MO) on MAC–GTE composite: (a) adsorption capacity over time; (b) efficiency over time; (c) adsorption capacity at varying pH; (d) efficiency at different pH levels. Note that the columns in (b) represent the removal efficiencies of MB and MO under their respective optimized initial concentrations (20 ppm for MB and 15 ppm for MO). These column values are not intended for direct comparison between the two dyes but to illustrate their individual adsorption behavior on the MAC–GTE composite.

it modifies into its azo structure.[50] When the pH rises, the surface becames deprotonated, which produced a negative charge on the composite. The electrostatic attractive forces develop between positively charged MB and negatively charged MAC-GTE which may cause dye improved adsorption effectiveness (98.29%) for MB at pH 9. This result suggests that the electrostatic repulsion among the negatively charged MAC–GTE's surface and the anionic MO dye molecules may have suppressed dye removal at high pH level.

3.5.2 Effect of initial concentration of dyes and sorbent dosage. The concentration effect of MB and MO was studied over the process of adsorption using various concentrations (10, 20, 30, and 40 ppm) and (15, 30, 45, and 60 ppm). Usually, adsorption effectiveness increases as the concentration increases, but % efficiency decreases due to a decrease in active sites for the process of adsorption. MB adsorption efficiency first increases to 20 ppm and then decreases as the concentration increases. The maximum efficiency for MB and MO was observed at 20 ppm and 10 ppm, respectively, while the adsorption capacity increased by 666.21 mg g^{-1} and 640 mg g^{-1}, respectively, as shown in Fig. 7a and b. As discussed in the literature for a given adsorbent dose, the total numbers of accessible adsorption sites are anchored, which means adsorbing nearly the same as the amount of adsorbate.[51]

The dye removal efficiency is increased due to the increased available adsorption sites and sorption surface.[52] Fig. 7c and d illustrate the adsorption pattern of MB and MO over different masses of composite (10, 15 mg), respectively. The increase in MB and MO uptake from 99.29% to 99.125 and 90.10 to 96.54% was accompanied by an increase in composite dosage, respectively. That is why the 10 mg dosage is suitable for further adsorptive experiments. Many open sites are responsible for enhancing percentage efficiency by increasing dosage. Both MB and MO quantity per unit mass of adsorbent is decreasing, which leads to a decrease in adsorption capacity. This increased mass shifts the adsorption process to the "screen effect", which prevents access to adsorption sites on adsorbent MO. Reports suggest that the accumulation of particles leads to a lessening in the number of active sites for adsorption.[53,54]

 © 2025 The Author(s). Published by the Royal Society of Chemistry

Open Access Article. Published on 25 November 2025. Downloaded on 1/19/2026 4:08:04 AM.
This article is licensed under a Creative Commons Attribution-NonCommercial 3.0 Unported Licence.

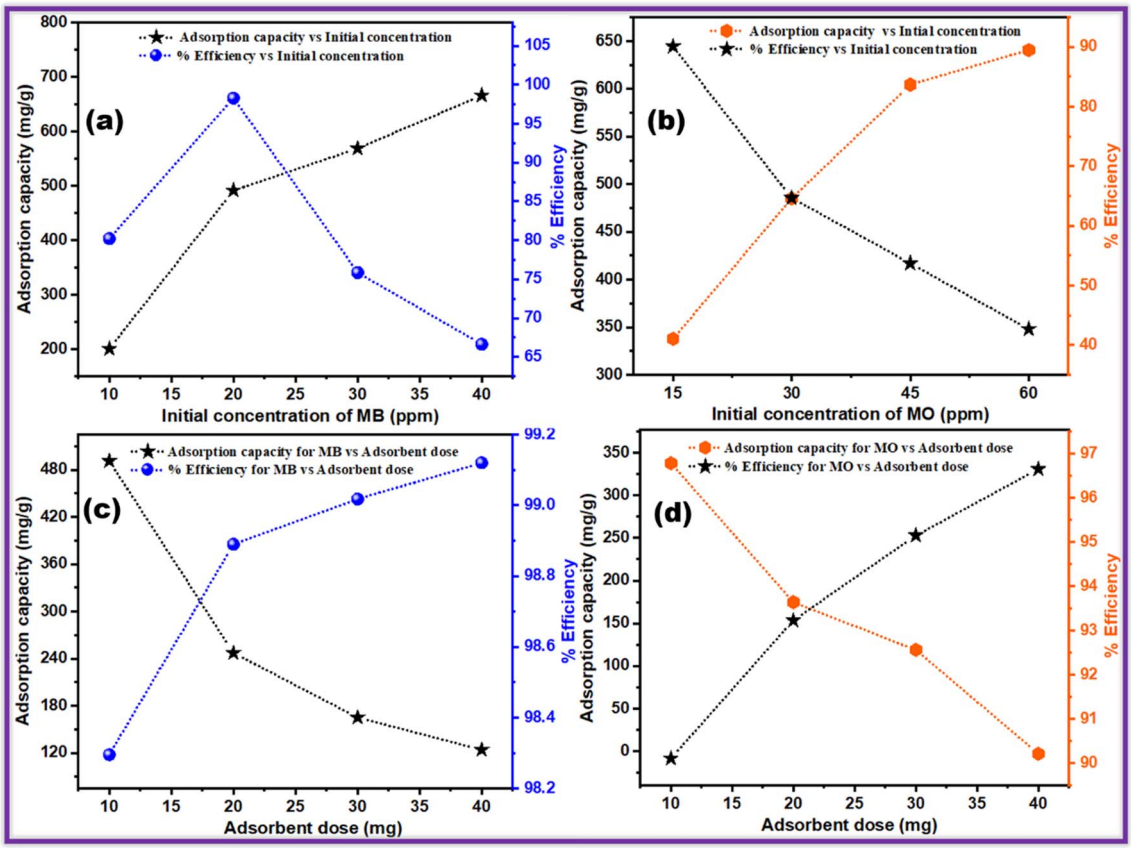

Fig. 7 Adsorption study of MB and MO on MAC-GTE composite. Effect of initial concentration on (a) MB and (b) MO; effect of adsorbent dose on adsorption capacity and % age removal efficiency for (c) MB and (d) MO.

3.5.3 Temperature studies and reusability tests. The high solution temperature increases the presence of surface-active sites and suppress the diffusion resistance of MB to nanocomposite, which promotes the adsorption, and the reported literature also confirms this augment.[55] The effect of temperature on the MB adsorption over the MAC–GTE composite was investigated using 20 ppm initial concentration and 10 mg of dosage at pH = 9, while MO sorption was analyzed by using 15 ppm concentration, 10 mg adsorbent mass at pH = 3. The temperature range was set to 298 K to 328 K, as shown in Fig. 8a.

It was noted that as the temperature rise from 15 to 25 °C, the removal efficiency of the MAC–GTE composite increased from 75.15% to 98.29% for MB and 67.6% to 90.10% for MO, which

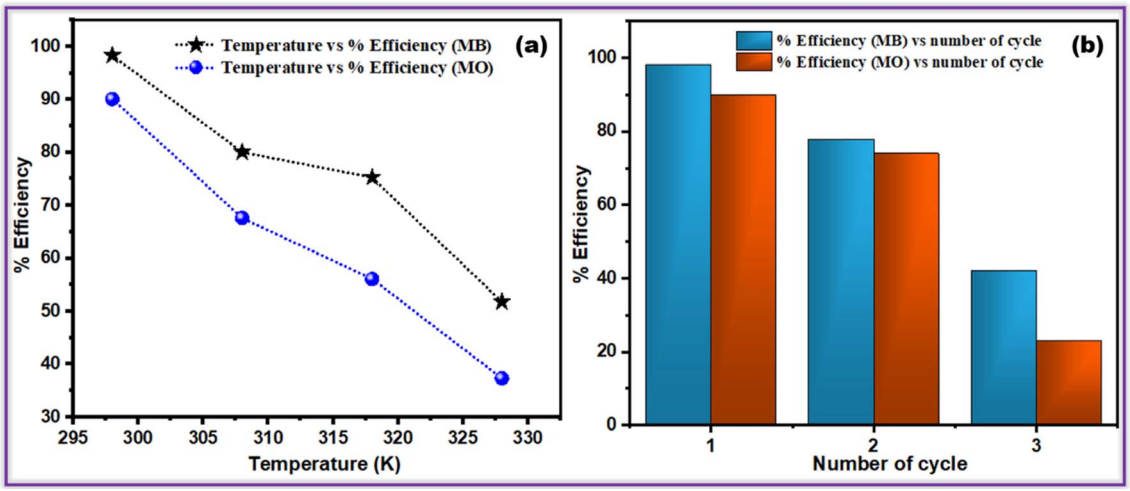

Fig. 8 Effect of (a) temperature and (b) cycling on adsorption of MB and MO on MAC–GTE composite.

Open Access Article. Published on 25 November 2025. Downloaded on 1/19/2026 4:08:04 AM.
This article is licensed under a Creative Commons Attribution-NonCommercial 3.0 Unported Licence.

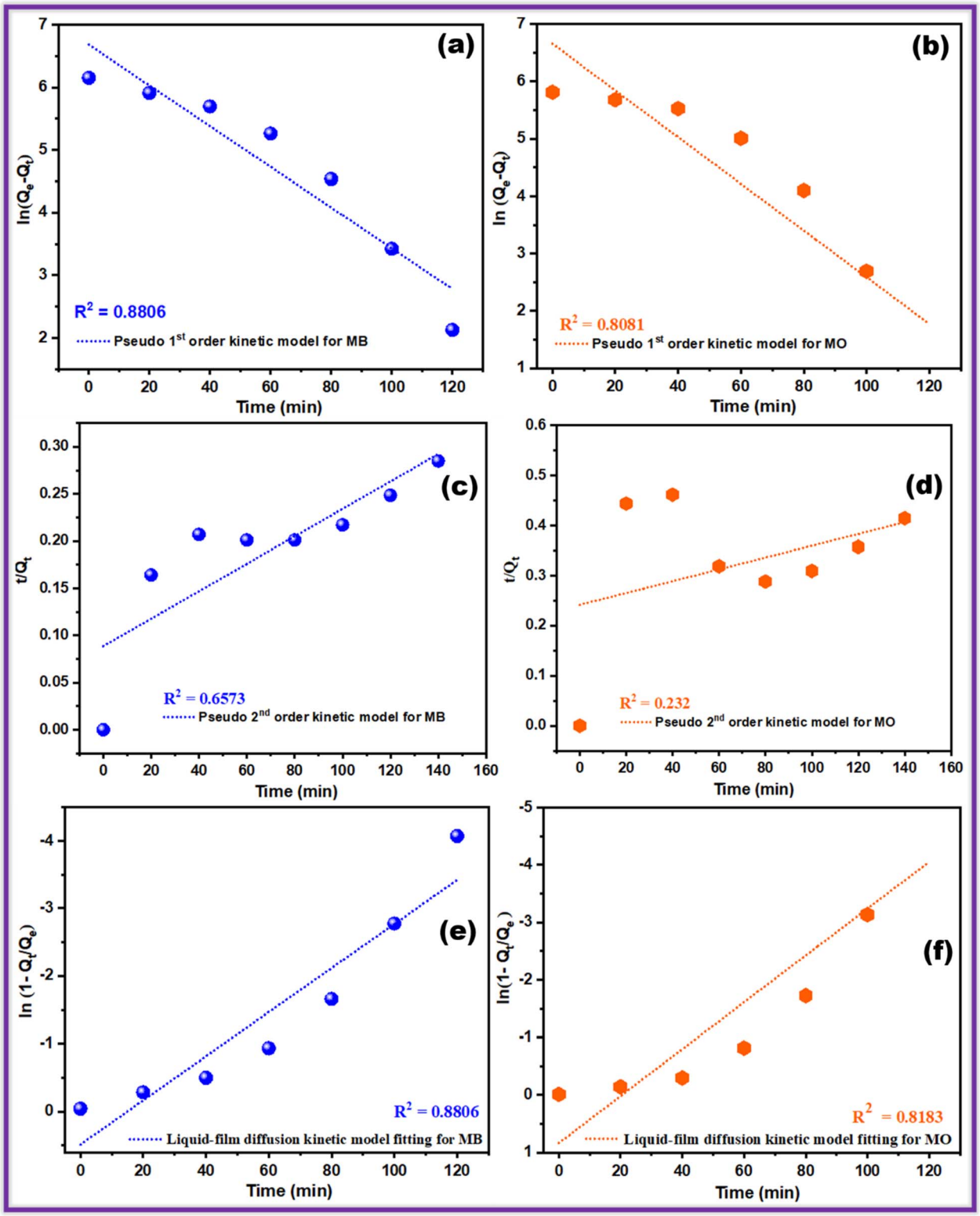

Fig. 9 Kinetic model fitting for MB and MO on MAC–GTE: (a) PFO for MB; (b) PFO for MO; (c) PSO for MB; (d) PSO for MO; (e) LFD for MB; (f) LFD for MO.

shows the adsorption mechanism based upon endothermic reaction. Another explanation could be that the MAC–GTE composite produces more active sites when the temperature rises, increasing dye adsorption. According to the findings, methylene blue and methyl orange at high temperatures have favorable, spontaneous, and endothermic adsorption on the MAC–GTE composite.

 © 2025 The Author(s). Published by the Royal Society of Chemistry

Open Access Article. Published on 25 November 2025. Downloaded on 1/19/2026 4:08:04 AM.
This article is licensed under a Creative Commons Attribution-NonCommercial 3.0 Unported Licence.

The reusability experiment was carried out with the following conditions: 10 mg adsorbent, 20 ppm solution of MB, and 15 ppm solution of MO in 250 mL, temperature 296 K and pH 9 for MB, and pH 3 for MO. Moreover, NaOH is employed as a reusability agent for washing adsorbate. Therefore, the utilized material was reused multiple times after magnetic separation, washing, and drying to know the reusability of MAC–GTE. The % efficiency for MB and MO decreases from 98.29 to 42.1 and 90.10 to 25.7 after three cycles, respectively, as depicted in Fig. 8b. It is clear that the adsorption efficiency decreases with the increase in the number of regeneration cycles (Fig. 8b), mainly because some active sites may be partially blocked by strongly bound dye molecules, while GTE-derived –OH and –COOH groups are also gradually lost during repeated washing and magnetic separation; these effects diminish the surface reactivity, a frequent behavior when bio-modified magnetic adsorbents undergo several cycles of reuse.

3.6 Kinetic study

The kinetic study of adsorption is critical for understanding the involving mechanism, particularly the movement/transport of the adsorbate (pollutants) from the liquid phase to the solid adsorbent surface.[56] The kinetic study of the adsorption effectiveness of MB and MO was simulated using PFO, PSO, and liquid film diffusion models, as shown in Fig. 9(a)–(f).

The regression constant value was determined by linear fitting to analyze the above models over adsorption. The regression constant (R^2) values for PFO, PSO, and LFD model for MB are (0.8806, 0.6573, and 0.8806) greater than the regression constant of the above model for MO. Table 1 shows the kinetic parameters of different models. The larger regression constant for PSO kinetic shows physical adsorption. The PFO model provided a more accurate description of the data than the PSO model. In addition to this, a large regression constant in the LFD kinetic model assists the adsorption process of the liquid and solid phases. Also, the diffusion of dye molecules in active sites of composite material paved the way for large adsorption capacity.

3.7 Adsorption isotherms

Several non-linear adsorption isotherm models, including Freundlich, Langmuir, and Temkin models, have been employed to explore the adsorption behavior.[57] The reported research validated that linear models introduce errors, notably when the data is not ideally linear.[58] It is clear from Fig. 10(a)–(f) that the Freundlich isothermal regression constant (R^2 = 0.9807, 0.9404) is larger than Langmuir's (R^2 = 0.9563, 0.8123) and Temkin's (R^2 = 0.9549, 0.1872) suggests that the Freundlich isotherm shows better fitting for characterizing the behavior of MAC–GTE in adsorbing MB and MO. This Freundlich isothermal fitting also indicates that the adsorption process is multilayer. While Langmuir provides a reasonable fit, the Freundlich model better describes the heterogeneous surface of MAC and MAC–GTE.

Furthermore, the above model's adsorption fitting had a determination coefficient R^2 that was very low in MO, which suggests that the above models do not verify the adsorption process for MO. Table 2 indicates the isothermal parameters of different isothermal models.

3.8 Adsorption mechanism

In order to investigate the adsorption mechanism, various possible interactions between MB, MO, and adsorbent are summarized. The adsorbent has aromatic ring structures that can interact with the aromatic rings of both MO and MB dyes to generate π–π interactions. In addition, the electrostatic interaction between the MO and adsorbent also contributed to the adsorption process. The major role was played by the π–π and O–H···π interactions between the dye molecules and adsorbent (Fig. 11). Functional groups such as $-NH_2$ on the adsorbent has possibility to enhance the binding.

Moreover, in literature, theoretical studies also support to understand the adsorption phenomena like adsorption kinetics, isotherm, thermodynamic study, and statistical analysis. Referring to the adsorption kinetics study, pseudo-first order, pseudo-second order, and the liquid-film diffusion models of MB and MO are appropriate for examining the absorption process due to values of R^2 0.8806, 0.8081, 0.6573, 0.232, 0.8806, 0.8183 respectively. Pseudo-first order and liquid-film diffusion models favor physical adsorption, while pseudo-second order favors the insertion of MB and MO in the porous surface of the adsorbent. Further, thermodynamic study assists in understanding the nature of the

Table 1 Kinetics parameters for adsorption of MB and MO on MAC–GTE composite

Pseudo-first-order model (MB)			Pseudo-second-order model (MB)			Liquid-film diffusion model (MB)		
Slope	K_1	R^2	Slope	K_2	R^2	Slope	K_F	R^2
−0.032	−0.0002	0.8806	0.00146	41 499.32	0.6573	0.011	−0.342	0.8806
Pseudo-first-order model (MO)			**Pseudo-second-order model (MO)**			**Liquid-film diffusion model (MO)**		
Slope	K_1	R^2	Slope	K_2	R^2	Slope	K_F	R^2
−0.04	−0.0002	0.8081	0.0012	167 361.2	0.232	0.0543	−0.783	0.8183

Open Access Article. Published on 25 November 2025. Downloaded on 1/19/2026 4:08:04 AM.
This article is licensed under a Creative Commons Attribution-NonCommercial 3.0 Unported Licence.

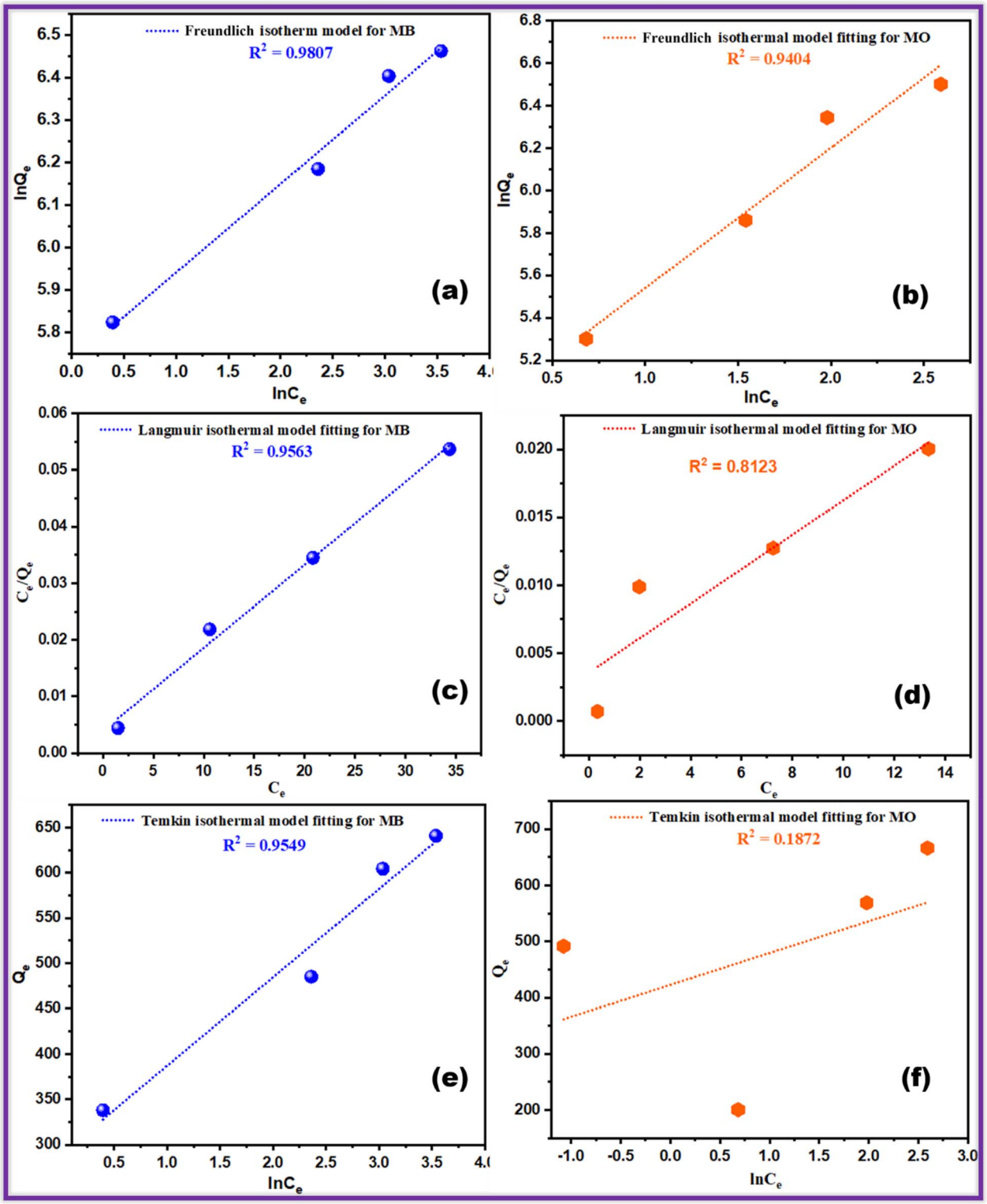

Fig. 10 Adsorption isotherm model fittings for MB and MO onto MAC–GTE composite using Freundlich (a and b), Langmuir (c and d), and Temkin (e and f) models.

adsorption workflow. Moreover, statistical analysis results for the adsorption of MB and MO on composite clarify the multilayered strategy adsorption process.

In addition, an outline of the maximum adsorption abilities (q_{max}) of distinct composite materials toward MB and MO in the form of comparison is depicted in Table 3.

 © 2025 The Author(s). Published by the Royal Society of Chemistry

Open Access Article. Published on 25 November 2025. Downloaded on 1/19/2026 4:08:04 AM.
This article is licensed under a Creative Commons Attribution-NonCommercial 3.0 Unported Licence.

Table 2 Isothermal parameters for adsorption of MB and MO on MAC–GTE composite

Freundlich isotherm (MB)			Langmuir isotherm (MB)			Tempkin isotherm (MB)		
Intercept	Slope	R^2	Intercept	Slope	R^2	Intercept	Slope	R^2
5.731	0.20874	0.9807	0.0039	0.0014	0.9563	289.34	97.56	0.9549
Freundlich isotherm (MO)			**Langmuir isotherm (MO)**			**Tempkin isotherm (MO)**		
Intercept	Slope	R^2	Intercept	Slope	R^2	Intercept	Slope	R^2
4.879	0.66	0.9404	0.0035	0.0012	0.8123	422.96	44.37	0.1872

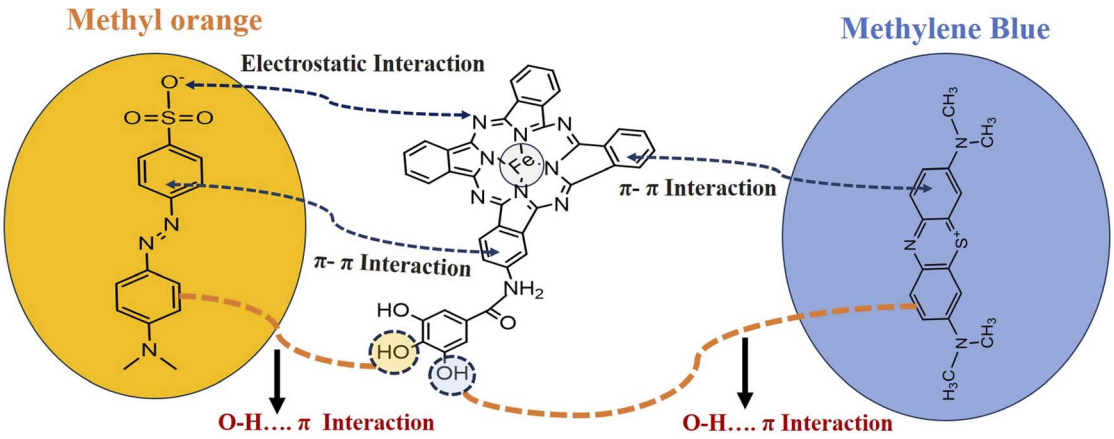

Fig. 11 Purposed adsorptive removal mechanisms for MB and MO on MAC–GTE composite.

Table 3 A comparative overview of the maximum adsorption abilities (q_{max}) of various composite material toward MB and MO

Materials	Adsorption capacity q_{max}, (mg g^{-1}) (MB)	Adsorption capacity q_{max}, (mg g^{-1}) (MO)	Mechanism	Ref.
MAC–GTE	491.47	337.89	Electrostatic interaction, O–H···π interaction, π–π interaction	This work
ZnO@AC	180.03	107.97	Electrostatic interaction, π–π interaction	59
CPML NC	471.12	230.87	Electrostatic interaction, π–π interaction, H-bonding	60
ACNPs	97.37	71.22	Electrostatic attraction and π–π interaction	61
DMCHA	349.68	325.42	Cation–π, electrostatic, π–π interactions	62
TiO_2/AC	0.452	0.329	Electrostatic interaction, π–π interaction, H-bonding	63
LSB-AC	185.2	140.8	π–π interaction-bonding	64
CHS-CSAC	217.35	105.2	Electrostatic interaction, π–π interaction, H-bonding	65
OLPAC	38	33	π–π interaction-bonding	66
PCA	1111	909	π–π interaction-bonding	67
HCNPs	203.4	113.3	Electrostatic interaction, π–π interaction, H-bonding	68

4. Conclusion

Under facile wet-chemical synthesis, green tea extract-derived magnetic activated carbon composite (MAC–GTE) material was prepared and characterized by various spectroscopes, PXRD, TGA, and SEM. We explored this material for the adsorption of organic dyes such as MB and MO, respectively. The optimum adsorption effectiveness of MB and MO were 98.29% and 90.10%, respectively. Additionally, the MAC–GTE composite showed excellent reusability and stability. The dye adsorption mechanisms are deeply analyzed. PSO fitted the removal of MB and MO, and the equilibrium study showed Freundlich isotherms, which revealed that the adsorption process is favorable at high temperature. Fabrication of the MAC–GTE composite was found to be the most effective adsorbent for decontamination of MB. These results have shown that the MAC–GTE composite has remarkable adsorption capability and selectivity, making it a promising material for environmental remediation. Green tea extract and magnetic activated carbon synergistically optimized the surface

Open Access Article. Published on 25 November 2025. Downloaded on 1/19/2026 4:08:04 AM.
This article is licensed under a Creative Commons Attribution-NonCommercial 3.0 Unported Licence.

properties, rendering an efficient and sustainable material for dye removal. This study puts into light the potential of MAC–GTE as a cost-effective, eco-friendly alternative to conventional adsorbents and as a promising material for environmental remediation. Further studies may look at scalability, regeneration, and application in real wastewater treatment.

Conflicts of interest

Authors do not have any conflict of interest.

Data availability

Data will be made available upon request.

Acknowledgements

Authors are thankful to their respective institutes for provide the research facilities.

References

1 F. Pan, S. Zhu, L. Shang, P. Wang, L. Liu and J. Liu, Assessment of drinking water quality and health risk using water quality index and multiple computational models: a case study of Yangtze River in suburban areas of Wuhan, central China, from 2016 to 2021, *Environ. Sci. Pollut. Res.*, 2024, **31**, 22736–22758.

2 S. Roy, J. Darabdhara and M. Ahmaruzzaman, Recent advances of copper-BTC metal-organic frameworks for efficient degradation of organic dye-polluted wastewater: synthesis, mechanistic insights and future outlook, *J. Hazard. Mater. Lett.*, 2024, **5**, 100094.

3 M. Hussain, M. Aadil, E. W. Cochran, S. Zulfiqar, W. Hassan, T. Kousar, H. H. Somaily and F. Mahmood, Facile synthesis of a porous sorbent derived from the rice husk biomass: a new and highly efficient material for water remediation, *Inorg. Chem. Commun.*, 2024, **160**, 112010.

4 M. S. Farooqi, M. Aadil, W. Hassan, M. R. Karim, H. Zaheer, M. Omair, M. S. Ali, K. H. Mahmoud and A. S. Alsubaie, Photocatalytic and antimicrobial activities of nanostructured bismuth oxide synthesis via the green route, *J. Indian Chem. Soc.*, 2024, **101**, 101270.

5 A. P. Periyasamy, Recent Advances in the Remediation of Textile-Dye-Containing Wastewater: Prioritizing Human Health and Sustainable Wastewater Treatment, *Sustainability*, 2024, **16**, 495.

6 H. A. Alsalmah, Green synthesis of copper doped bismuth oxide: a novel inorganic material for photocatalytic mineralization of Trypan blue dye, *Inorg. Chem. Commun.*, 2024, **163**, 112270.

7 Z. Ali, M. Aadil, B. zainab, M. H. Rasool, W. Hassan, S. Mubarik, Z. Ahmad, N. A. Almuhous, A. A. Alothman and M. Hussain, Synthesis of nanostructured In2O3 ceramics via a green and chemical method for the mineralization of crystal violet dye: a comparative study, *Inorg. Chem. Commun.*, 2023, **157**, 111399.

8 R. Al-Tohamy, S. S. Ali, F. Li, K. M. Okasha, Y. A.-G. Mahmoud, T. Elsamahy, H. Jiao, Y. Fu and J. Sun, A critical review on the treatment of dye-containing wastewater: ecotoxicological and health concerns of textile dyes and possible remediation approaches for environmental safety, *Ecotoxicol. Environ. Saf.*, 2022, **231**, 113160.

9 S. H. Teo, C. H. Ng, A. Islam, G. Abdulkareem-Alsultan, C. G. Joseph, J. Janaun, Y. H. Taufiq-Yap, S. Khandaker, G. J. Islam, H. Znad and M. R. Awual, Sustainable toxic dyes removal with advanced materials for clean water production: a comprehensive review, *J. Clean. Prod.*, 2022, **332**, 130039.

10 H. Alkhaldi, S. Alharthi, S. Alharthi, H. A. AlGhamdi, Y. M. AlZahrani, S. A. Mahmoud, L. G. Amin, N. H. Al-Shaalan, W. E. Boraie, M. S. Attia, S. A. Al-Gahtany, N. Aldaleeli, M. M. Ghobashy, A. I. Sharshir, M. Madani, R. Darwesh and S. F. Abaza, Sustainable polymeric adsorbents for adsorption-based water remediation and pathogen deactivation: a review, *RSC Adv.*, 2024, **14**, 33143–33190.

11 D. Dimbo, M. Abewaa, E. Adino, A. Mengistu, T. Takele, A. Oro and M. Rangaraju, Methylene blue adsorption from aqueous solution using activated carbon of Spathodea campanulata, *Results Eng.*, 2024, **21**, 101910.

12 J. El Gaayda, F. E. Titchou, R. Oukhrib, I. Karmal, H. A. Oualid, A. Berisha, H. Zazou, C. Swanson, M. Hamdani and R. A. Akbour, Removal of cationic dye from coloured water by adsorption onto hematite-humic acid composite: experimental and theoretical studies, *Sep. Purif. Technol.*, 2022, **288**, 120607.

13 M. F. Hanafi and N. Sapawe, A review on the water problem associate with organic pollutants derived from phenol, methyl orange, and Remazol brilliant blue dyes, *Mater. Today: Proc.*, 2020, **31**, A141–A150.

14 Y. S. Reddy, N. K. Rotte, B. K. Sudhakar, N. R. Chand, R. J. Naik, S. Mandal and M. R. Chandra, Biomass-derived sustainable mesoporous activated carbon as an efficient and recyclable adsorbent for the adsorption of hazardous dyes, *Hybrid Adv.*, 2024, **6**, 100218.

15 G. Sharma, S. Sharma, A. Kumar, C. W. Lai, M. Naushad, Shehnaz, J. Iqbal and F. J. Stadler, Activated carbon as superadsorbent and sustainable material for diverse applications, *Adsorpt. Sci. Technol.*, 2022, **2022**, 4184809.

16 B. Qiu, Q. Shao, J. Shi, C. Yang and H. Chu, Application of biochar for the adsorption of organic pollutants from wastewater: modification strategies, mechanisms and challenges, *Sep. Purif. Technol.*, 2022, **300**, 121925.

17 A. T. Alves, D. J. Lasmar, I. P. d. A. Miranda, J. d. S. Chaar and J. d. S. Reis, The potential of activated carbon in the treatment of water for human consumption, a study of the state of the art and its techniques used for its development, *Adv. Biosci. Biotechnol.*, 2021, **12**, 143–153.

18 I. Pet, M. N. Sanad, M. Farouz, M. M. ElFaham, A. El-Hussein, M. S. A. El-sadek, R. A. Althobiti and A. Ioanid, Review: Recent Developments in the Implementation of

 © 2025 The Author(s). Published by the Royal Society of Chemistry

Open Access Article. Published on 25 November 2025. Downloaded on 1/19/2026 4:08:04 AM.
This article is licensed under a Creative Commons Attribution-NonCommercial 3.0 Unported Licence.

Activated Carbon as Heavy Metal Removal Management, *Water Conserv. Sci. Eng.*, 2024, **9**, 62.

19 S. Lilhare, S. B. Mathew, A. K. Singh and S. A. Carabineiro, Aloe vera functionalized magnetic nanoparticles entrapped Ca alginate beads as novel adsorbents for Cu (II) removal from aqueous solutions, *Nanomaterials*, 2022, **12**, 2947.

20 A. Venkatachalam, J. P. Jesuraj and K. Sivaperuman, Moringa oleifera Leaf Extract-Mediated Green Synthesis of Nanostructured Alkaline Earth Oxide (MgO) and Its Physicochemical Properties, *J. Chem.*, 2021, **2021**, 4301504.

21 L. Soltys, O. Olkhovyy, T. Tatarchuk and M. Naushad, Green synthesis of metal and metal oxide nanoparticles: principles of green chemistry and raw materials, *Magnetochemistry*, 2021, **7**, 145.

22 O. Cioanca, I.-I. Lungu, I. Mita-Baciu, S. Robu, A. F. Burlec, M. Hancianu and F. Crivoi, Extraction and purification of catechins from tea leaves: an overview of methods, advantages, and disadvantages, *Separations*, 2024, **11**, 171.

23 F. Munawar, M. Khalid, M. Imran, M. N. Qasim, S. Waseem, M. A. AlDamen, M. Ashfaq, M. Imran and M. N. Akhtar, An Oxalato-Bridged Cu(II)-Based 1D Polymer Chain: Synthesis, Structure, and Adsorption of Organic Dyes, *Polymers*, 2024, **16**, 1742.

24 R. Zhong, H. Lyu, X. Su, X. Yan, Y. Teng, W. Dong, Y. Wan, T. Song and X. Shen, Freeze–thaw–induced regulation of petroleum hydrocarbon adsorption in cold-region soils: role of organic matter dynamics, *Water Res.*, 2025, **287**, 124495.

25 S. Li, X. Zhang and Y. Huang, Zeolitic imidazolate framework-8 derived nanoporous carbon as an effective and recyclable adsorbent for removal of ciprofloxacin antibiotics from water, *J. Hazard. Mater.*, 2017, **321**, 711–719.

26 N. Ayawei, A. N. Ebelegi and D. Wankasi, Modelling and Interpretation of Adsorption Isotherms, *J. Chem.*, 2017, **2017**, 3039817.

27 N. Mushahary, A. Sarkar, B. Das, S. L. Rokhum and S. Basumatary, A facile and green synthesis of corn cob-based graphene oxide and its modification with corn cob-K2CO3 for efficient removal of methylene blue dye: adsorption mechanism, isotherm, and kinetic studies, *J. Indian Chem. Soc.*, 2024, **101**, 101409.

28 D. Shrestha, Tailored Bombax ceiba-based activated carbons for enhanced rhodamine B removal: a sustainable approach to industrial effluent remediation, *Asian J. Water Environ. Pollut.*, 2025, **22**, 187–204.

29 P. Negi and A. Kumar, MoS2 nanoparticle/activated carbon composite as a dual-band material for absorbing microwaves, *Nanoscale Adv.*, 2021, **3**, 4196–4206.

30 L. C. R. dos Santos, L. Bach-Toledo, G. M. M. M. Lustosa, B. A. Bregadiolli, W. A. Bizzo and T. Mazon, Polyurethane matrix as an oxide@biochar composite supports employed in heterogeneous photocatalysis, *J. Indian Chem. Soc.*, 2025, **102**, 101559.

31 M. A. Ashraf, J. Wiener, A. Farooq, J. Saskova and M. T. Noman, Development of maghemite glass fibre nanocomposite for adsorptive removal of methylene blue, *Fibers Polym.*, 2018, **19**, 1735–1746.

32 Y. Muniandy, S. Mohamad and M. Raoov, Green and efficient magnetic micro-solid phase extraction utilizing tea waste impregnated with magnetic nanoparticles for the analysis of ibuprofen in water samples by using UV-vis spectrophotometry, *RSC Adv.*, 2024, **14**, 11977–11985.

33 A. Doi, M. Ganguly and P. Sharma, Novel environmental applications of green tea: sensing and remediation of Ag+ in aqueous system, *RSC Adv.*, 2024, **14**, 31243–31250.

34 L. Xu, L. Zhang, D. Ren, Y. Peng, Z. Liu, Y. Meng, W. Deng and Y. Zhang, Green synthesis of Cu/Fe3O4 nanoparticles using green tea extract: evaluation of its catalytic activity, antioxidant and anti-colon cancer effects, *Inorg. Chem. Commun.*, 2022, **144**, 109927.

35 M. Kawsar, M. S. Hossain, N. M. Bahadur and S. Ahmed, Synthesis of nano-crystallite hydroxyapatites in different media and a comparative study for estimation of crystallite size using Scherrer method, Halder-Wagner method size-strain plot, and Williamson-Hall model, *Heliyon*, 2024, **10**, e25347.

36 M. Rashid, W. Hassan, M. Aadil, H. H. Somaily, N. M. Mahdi, R. Lataef, A. G. Taki, K. Srithilat, D. F. Baamer, S. M. Albukhari, M. A. Salam and A. llyas, Solar-light-driven and magnetically recoverable doped nano-ferrite: an ideal photocatalyst for water purification applications, *Opt. Mater.*, 2023, **135**, 113192.

37 G. Nazik, M. Aadil, S. Zulfiqar, W. Hassan, A. Rahman, S. M. Ibrahim, K. Naseem, T. A. Sheikh and M. N. Akhtar, Synthesis of doped metal sulfide nanoparticles and their graphene reinforced nanohybrid for Pb(II) detection, *Z. Phys. Chem.*, 2023, **237**, 1257–1285.

38 N. Kumar, R. Gusain, S. Pandey and S. S. Ray, Hydrogel nanocomposite adsorbents and photocatalysts for sustainable water purification, *Adv. Mater. Interfaces*, 2023, **10**, 2201375.

39 J. Naseem, M. A. Rafea, M. E. A. Zaki, M. I. Attia, M. R. El-Aassar, F. Alresheedi, S. Zulfiqar and M. Aadil, Combining nanotechnology and nanohybrid methods to improve the physical and chemical properties of CuS and boost its photocatalytic aptitude, *RSC Adv.*, 2025, **15**, 13940–13950.

40 I. Ayman, M. Aadil, B. A. Alwan, H. Khemira, S. Zulfiqar, A. Khalid, Z. M. Aldhafeeri and M. F. Warsi, Surfactant-mediated wet-chemical synthesis of magnetically retrievable and structurally tuned cobalt ferrite: a visible light-triggered photocatalyst for the abatement of azo dye, *Inorg. Chem. Commun.*, 2025, **174**, 113988.

41 M. Moheb, A. M. El-Wakil and F. S. Awad, Highly porous activated carbon derived from the papaya plant (stems and leaves) for superior adsorption of alizarin red s and methylene blue dyes from wastewater, *RSC Adv.*, 2025, **15**, 674–687.

42 P. S. Devi, S. N. Chanu, P. Dasgupta, B. S. Swain and B. P. Swain, Structural, optical, thermal and electrochemical properties of rGO/PEDOT:PSS/PVP composite for supercapacitor electrode application, *Appl. Phys. A: Mater. Sci. Process.*, 2022, **128**, 403.

43 Q. Ma, Y. Qian, W. Su, L. Shi, E. Wang, A. Yu, J. Zheng and Y. Lu, Degradation of agricultural polyethylene film by

Open Access Article. Published on 25 November 2025. Downloaded on 1/19/2026 4:08:04 AM.
This article is licensed under a Creative Commons Attribution-NonCommercial 3.0 Unported Licence.

greater wax moth (Galleria mellonella) larvae and screening of involved gut bacteria, *Ecotoxicol. Environ. Saf.*, 2025, **303**, 118841.

44 B. K. Sodipo, O. A. Noqta, A. A. Aziz, M. Katsikini, F. Pinakidou and E. C. Paloura, Influence of capping agents on fraction of Fe atoms occupying octahedral site and magnetic property of magnetite (Fe3O4) nanoparticles by one-pot co-precipitation method, *J. Alloys Compd.*, 2023, **938**, 168558.

45 Z. Cao, Z. Pan and Z. Chen, A comparative study on in situ synthesis of two iron nanoparticles in acid mine drainage using green tea and Excoecaria cochinchinensis leaves extracts, *Chemosphere*, 2025, **381**, 144488.

46 H. T. Hamzah, V. Sridevi, D. V. Surya, S. Palla, A. Yadav and P. V. Rao, Conventional and microwave-assisted acid pretreatment of tea waste powder: analysis of functional groups using FTIR, *Environ. Sci. Pollut. Res.*, 2024, **31**, 57523–57532.

47 R. Anaya, M. B. Carranza, F. Booth, M. F. Hernández, A. Mocciaro, D. Richard and N. M. Rendtorff, Low-density kaolinitic ceramic proppants based on rice husk ash, *Ceram. Int.*, 2025, **51**, 25473–25486.

48 A. K. Mondal, C. Hinkley, L. Krishnan, N. Ravi, F. Akter, P. Ralph and U. Kuzhiumparambil, Macroalgae-based biochar: preparation and characterization of physicochemical properties for potential applications, *RSC Sustain.*, 2024, **2**, 1828–1836.

49 L. Baloo, M. H. Isa, N. B. Sapari, A. H. Jagaba, L. J. Wei, S. Yavari, R. Razali and R. Vasu, Adsorptive removal of methylene blue and acid orange 10 dyes from aqueous solutions using oil palm wastes-derived activated carbons, *Alex. Eng. J.*, 2021, **60**, 5611–5629.

50 H. Zhu, R. Jiang, L. Xiao and G. Zeng, Preparation, characterization, adsorption kinetics and thermodynamics of novel magnetic chitosan enwrapping nanosized γ-Fe2O3 and multi-walled carbon nanotubes with enhanced adsorption properties for methyl orange, *Bioresour. Technol.*, 2010, **101**, 5063–5069.

51 S. I. H. Taqvi, S. M. Hasany and M. I. Bhanger, Sorption profile of Cd(II) ions onto beach sand from aqueous solutions, *J. Hazard. Mater.*, 2007, **141**, 37–44.

52 S. Wang and H. Li, Kinetic modelling and mechanism of dye adsorption on unburned carbon, *Dyes Pigm.*, 2007, **72**, 308–314.

53 M. Ahmaruzzaman, MXenes and MXene based nanocomposites: a new generation potential materials for removal of organic contaminants from water, *Int. J. Environ. Anal. Chem.*, 2024, **104**, 3026–3042.

54 A. Q. Alorabi, M. S. Hassan and M. Azizi, Fe3O4-CuO-activated carbon composite as an efficient adsorbent for bromophenol blue dye removal from aqueous solutions, *Arab. J. Chem.*, 2020, **13**, 8080–8091.

55 S. Atta, A. Siddique, M. N. Qasim, M. A. Aldamen, T. A. Sheikh, N. A. Sadullayevich and M. N. Akhtar, Perchlorate-supported Cu(II)-based 1D polymeric chains containing 1,10-phenanthroline: synthesis, characterization and adsorption of organic dyes and heavy metal ions, *CrystEngComm*, 2025, **27**, 1346–1362.

56 N. Can, Electrospun CuO nanofibers for room temperature volatile organic compound sensing applications, *Mater. Chem. Phys.*, 2018, **213**, 6–13.

57 E. Hussain, M. Sultana, M. Z. Abid, A. K. Buzdar, H. K. Thabet, S. M. El-Bahy, M. Jalil, A. Rauf, Z. M. El-Bahy and K. Rafiq, A report on arsenic removal from water via adsorption of an arsenomolybdate complex on S–CuFe2O4 adsorbents, *Environ. Sci.: Water Res. Technol.*, 2024, **10**, 2030–2047.

58 S. Devi, Aarushi and S. Tyagi, Porous zinc-discs as nanocatalysts for methylene blue dye treatment in water: sensing, adsorption and photocatalytic degradation, *RSC Adv.*, 2022, **12**, 34951–34961.

59 W. Ahlawat, N. Dilbaghi, R. Kumar, N. K. Singhal, A. Kaushik and S. Kumar, Adsorption of harmful dyes and antimicrobial studies utilizing recyclable ZnO, its composites with conventionally used activated carbon, and waste orange peel as a greener approach, *J. Environ. Chem. Eng.*, 2023, **11**, 110268.

60 M. S. Rostami and M. M. Khodaei, Chitosan-based composite films to remove cationic and anionic dyes simultaneously from aqueous solutions: modeling and optimization using RSM, *Int. J. Biol. Macromol.*, 2023, **235**, 123723.

61 D. Pathania, A. Araballi, F. Fernandes, J. M. Shivanna, G. Sriram, M. Kurkuri, G. Hegde and T. M. Aminabhavi, Cost effective porous areca nut carbon nanospheres for adsorptive removal of dyes and their binary mixtures, *Environ. Res.*, 2023, **224**, 115521.

62 A. Lv, X. Lv, X. Xu, Y. Chen, J. Zhang and Z.-B. Shao, Tailored multifunctional composite hydrogel based on chitosan and quaternary ammonium ionic liquids@ montmorillonite with different chain lengths for effective removal of dyes and 4-nitrophenol, *Sep. Purif. Technol.*, 2024, **342**, 127019.

63 N. T. T. Tu, T. S. Thanh, P. T. Quy, T. T. M. Ha, P. T. K. Thu, N. H. Bich, L. V. T. Sơn, V. T. Nguyen, D. N. Nhiem and P. K. Lieu, Trinary component adsorption of methylene blue, methyl orange, and methyl red from aqueous solution using TiO2/activated carbon, *Adsorpt. Sci. Technol.*, 2023, **2023**, 8943198.

64 A. M. Zayed, B. S. Metwally, M. Masoud, M. F. Mubarak, H. Shendy, P. Petrounias and M. S. A. Wahed, Facile synthesis of eco-friendly activated carbon from leaves of sugar beet waste as a superior nonconventional adsorbent for anionic and cationic dyes from aqueous solutions, *Arab. J. Chem.*, 2023, **16**, 104900.

65 A. S. Kamdod and M. V. P. Kumar, Adsorption of methylene blue, methyl orange, and crystal violet on microporous coconut shell activated carbon and its composite with chitosan: isotherms and kinetics, *J. Polym. Environ.*, 2022, **30**, 5274–5289.

66 D. Ramutshatsha-Makhwedzha, A. Mavhungu, M. L. Moropeng and R. Mbaya, Activated carbon derived from waste orange and lemon peels for the adsorption of

 © 2025 The Author(s). Published by the Royal Society of Chemistry

Open Access Article. Published on 25 November 2025. Downloaded on 1/19/2026 4:08:04 AM.
This article is licensed under a Creative Commons Attribution-NonCommercial 3.0 Unported Licence.

methyl orange and methylene blue dyes from wastewater, *Heliyon*, 2022, **8**, e09930.

67 M. Chegeni, S. Etemadpour and M. H. Fekri, The perlite-calcium alginate-activated carbon composite as an efficient adsorbent for the removal of dyes from aqueous solutions, *Phys. Chem. Res.*, 2021, **9**, 1–16.

68 N. Hamad, A. A. Galhoum, A. Saad and S. Wageh, Efficient adsorption of cationic and anionic dyes using hydrochar nanoparticles prepared from orange peel, *J. Mol. Liq.*, 2024, **409**, 125349.